P3-11

Stochastic transport modeling of resonant magnetic perturbations in DIII-D

I. Joseph[a*], R.A. Moyer[a], T.E. Evans[b], M.J. Schaffer[b], A.M. Runov[c], R. Schneider[c], S.V. Kasilov[d], M. Groth[e], and M.E. Fenstermacher[e]

[a]University of California-San Diego, La Jolla, California, USA

[b]General Atomics, P.O. Box 85608, San Diego, California, USA

[c]Max Planck Institut für Plasmaphysik, EURATOM Association, Teilinstitut Greifswald, Germany

[d]Institute of Plasma Physics, Kharkov Institute of Physics and Technology, Kharkov, Ukraine

[e]Lawrence Livermore National Laboratory, Livermore, California, USA

Three-dimensional two-fluid simulations of heat transport due to resonant magnetic perturbations of tokamaks have been computed by coupling the TRIP3D field line tracing code to the E3D edge transport code. The predicted electron temperature contours follow the new separatrix represented by the perturbed invariant manifold structure of the X-point in qualitative agreement with X-point TV observations. However, preliminary modeling predicts that the resulting stochastic heat transport is greater than that measured in low-collisionality ELM suppression experiments in DIII-D H-mode plasmas. While improved determination of transport coefficients is needed, possible explanations include plasma screening of resonant perturbations, limitations of the treatment of the edge as a fluid, or insufficient understanding of stochastic heat transport.

JNM Keywords: M0200, P0500, P0600, T0100

PSI Keywords: DIII-D, 3D fluid code, edge modeling, stochastic boundary, ELM control

PACS: 05.45.Gg, 52.55.Fa, 52.55.Rk, 52.65.-y

*Corresponding author: Ilon Joseph, General Atomics, P.O. Box 85608, MS 13-368, San Diego, California 92186-5608

e-mail: ijoseph@ucsd.edu

Presenting author and e-mail: Same as Corresponding author

1. Introduction

Recent DIII-D experimental results [1-4] have shown that the addition of small resonant magnetic perturbations (RMPs), $\langle \delta b / B \rangle_{res} \sim 10^{-4}$, to the edge of a tokamak can suppress edge localized mode (ELM) instabilities in H-modes over a wide range of collisionality. In order to provide detailed modeling of the effect of the perturbed magnetic field on DIII-D equilibria, a new tool for calculating fully three-dimensional heat transport in resonantly perturbed tokamaks has been created by coupling the TRIP3D magnetic field line tracing code [5] to the E3D two-fluid transport code [6,7]. Although more complete physical modeling is still necessary, such calculations could be used to predict plasma profiles and, in turn, assess the performance of RMP-based ELM suppression strategies for new devices like ITER.

TRIP3D models the magnetic field as a superposition of the axisymmetric equilibrium fields calculated by the EFIT Grad-Shafranov solver [8] and the non-axisymmetric fields produced by models of DIII-D's measured field errors, error-correction coils (C-coil), and MHD control coils (I-coil). Under typical, $n = 3$ I-coil operating conditions characteristic of the low-collisionality ELM control experiments [3,4], the relatively strong RMPs are predicted to produce stochasticity over the outer 25% of the flux surfaces and allow field lines to directly escape over the last 5-10% of flux surfaces (cf. Fig. 1) in the absence of any significant plasma response. E3D computes the detailed electron and ion temperature profiles resulting from the 3D magnetic geometry specified by TRIP3D field model and an appropriate set of plasma/boundary conditions. E3D models the plasma as a quasi-neutral Braginskii two-fluid with anomalous perpendicular transport coefficients. The code has been used to model the TEXTOR tokamak's dynamic ergodic divertor [6] and to make predictions for the W7-X stellarator [7]. Aside from the specialized (Monte-Carlo) numerical techniques required for accurate 3D computation, E3D works like a three-dimensional version of the axisymmetric UEDGE [9] and B2 [10] edge-modeling codes.

2. Computational Results

For our simulations, we focus on the electron temperature profiles in the low-density plasma discharge #122342 at 4650 ms after ELMs have been completely eliminated by applying the $n = 3$ I-coil [3,4]. Figure 1 shows a Poincaré plot of field line trajectories for 1000 toroidal transits produced by TRIP3D including the I-coil (3 kA) and C-coil (12 kAt). Also shown are the EFIT flux surfaces, DIII-D vacuum vessel, and I-coil positions. The I-coil alone produces a strong RMP in this so-called "even-parity" configuration where the current in the upper and lower coils (red circles in Fig. 1) circulate in the same direction at each toroidal location. Thus, we explore the changes to the temperature profile and heat flux deposition as the strength of the I-coil current is varied from 0 to 3 kA.

The TRIP3D magnetic field model superimposes the vacuum magnetic fields produced by the I-coil and C-coil over an axisymmetric EFIT equilibrium. The E3D code uses Monte-Carlo integration to solve the advection-diffusion equation for temperature by tracking the Brownian motion of heat packets. It efficiently treats the highly anisotropic heat conductivity that produces strong parallel transport by working in multiple local magnetic coordinate systems [6] that follow the three-dimensional field line motion. Improved efficiency is obtained by using a set of local Boozer-like coordinates [7] that remove the majority of the parallel spatial dependence of the transport coefficients $\chi_{e,i}$. In the simulations, we use realistic wall geometry with sheath boundary conditions.

Although the density at the edge of an H-mode critically depends on the physics of neutral penetration [11], it is not modeled in this version of E3D. Instead, a fixed density profile is imposed which only roughly matches the experimental Thomson data where $n_e = 2\times10^{19}$ m^{-3} on the inner surface, linearly drops to $n_e = 4\times10^{18}$ m^{-3} near the EFIT separatrix, and is taken to be constant everywhere outside the separatrix. Since the actual density achieved varies with I-coil strength, we are not simulating actual discharges, but

performing a numerical experiment to investigate the variation of pedestal temperature with applied perturbation strength for a fixed density profile.

As a fluid code, the region of validity is confined to the plasma edge; however, since the current E3D implementation requires the inner boundary to be a good closed flux surface, for the majority of the runs, our inner boundary is set to the inner edge of the pedestal, a normalized poloidal flux of $\psi_n = 77\%$, where we use fixed temperature boundary conditions: $T_e = 1.6$ keV and $T_i = 2.6$ keV. Near this inner surface, the plasma is highly collisionless and the plasma a kinetic description may be required. In the simulations below, we have chosen $\chi_{\perp,e} = \chi_{\perp,i} = 0.2$ m^2/s constant throughout the domain. These values are found to match the experimental temperature profile from Thomson scattering data reasonably well for the case of axisymmetric fields without perturbation and are consistent with previous experimental and computational studies of H-mode transport coefficients [12]. However, the coefficients are too small on the inner boundary resulting in a poor match to the measured input power. High fidelity modeling will require preliminary 1D/2D transport analyses in order to determine the spatial variation of the transport coefficients with higher accuracy.

Under perturbation, the separatrix of a poloidally diverted tokamak becomes a so-called "homoclinic tangle" [13,14]. The X-point will survive the perturbation, but it now consists of two separate branches of field-line invariant manifolds satisfying $\boldsymbol{B} \cdot \nabla \psi = 0$. The forward stable (or backward unstable) manifold consists of all field lines that asymptotically approach the X-point in the positive toroidal direction while the forward unstable (or backward stable) manifold consists of all field lines that asymptotically approach the X-point in the opposite direction. Figure 2 compares the predicted electron temperature profile with the invariant manifolds that enter/exit the X-point calculated directly from field line mapping. The simulations demonstrate that the temperature contours closely follow a combination of both manifolds in order to ensure $\boldsymbol{B} \cdot \nabla \boldsymbol{T} \approx 0$. When the folds of this new separatrix grow large

enough to intersect the divertor target plate at well-separated positions, they can cause the divertor strike point to split into multiple helical stripes. D_α filtered tangential X-point TV images show a dramatic change from a single stripe to multiple stripes on the inner strike point (Fig. 3) during the n = 3 even-parity I-coil current pulse in shot #123301. The calculated width of 5 cm is in good agreement with the observations. Previous experimental signatures of this phenomenon have been reported in Refs. 14–15.

E3D predictions for the electron temperature across the pedestal are shown as a function of normalized poloidal flux, ψ_n, in Figs. 4 and 5 as the I-coil current is successively raised from 0 to 3 kA. The electron temperature profile clearly cools and relaxes over the stochastic region as the perturbation strength is raised and shows that large temperature gradients can only be sustained over regions with good flux surfaces. In contrast, the measured T_e profile, shown in Fig. 5 for the 3 kA case, has a slightly higher pedestal and steeper gradient than the zero-current case. The experimental input power was essentially unchanged after energizing the I-coil, while the simulated input power was increased by a factor of 2.5 as the I-coil was turned on to full strength. The average heat flux through the divertor legs increases by a factor of 2 while the width of the divertor footprints increase by a factor of 1.25; thus, the predicted thermal conductance of the edge + divertor plasma increased by a factor of 2.5. The lowest curve in Fig. 5 (purple) shows the effect of adding the C-coil at a current of 12 kAt (about 1 m from the plasma). Since the flux surfaces are destroyed outside of ψ_n = 65% as shown in the Poincaré plot in Fig. 1, for this run the inner boundary was set to ψ_n = 63%.

3. Discussion

In contrast to the original moderate-collisionality, $\nu_e^* \sim 1$, odd-parity experiments [1,2] where large Type-I ELMs were replaced by a small transport event regime, the more recent low-collisionality, $\nu_e^* \sim 0.1$, even-parity experiments [3,4] achieved complete ELM suppression. Since roughly the same stored energy was achieved for the same neutral beam

injection (NBI) power, the energy losses due to ELMs must be replaced by another type of transport process either directly or indirectly generated by the RMP. Complete ELM elimination in these cases is only observed within a range of edge q, qualitatively consistent with a resonant transport process such as field line stochasticity, but with a window, $q_{95} \sim$ 3.5–3.7, that appears too narrow for the applied perturbation spectrum. In contrast with the theory of stochastic transport [16], the experimental electron temperature achieves the same pedestal height and its gradient actually increases across the transport barrier [4], although there is significant flattening of the profile at the top of the pedestal. The most significant change to the measured Thomson profiles is actually a large drop in core density which reduces the pedestal to ITER-relevant collisionality. In fact, in Ref. 3 it is shown that it is largely the drop in pedestal density that lowers the pressure gradient below the ELM stability threshold.

Although the simulation results demonstrate that the temperature profiles closely follow the invariant manifolds [13], the calculated stochastic heat loss is too great to match the low-collisionality experimental results in Refs. 3–4. However, the current 3D simulations are still at the preliminary stages of adding the physics required to quantitatively model H-mode plasmas: parallel flow, electric field, neutral penetration, impurities, etc, and require more accurate determination of turbulent transport coefficients and specification of density profile. Ultimately, any model of RMP-induced transport must capture the clearest change in the experiment: increased particle transport. The loss of particles without reducing temperature may suggest convection, but kinetic effects such as enhanced trapped particle losses due to islands may play a significant role.

The simple approximation of adding the RMP fields in vacuum to an axisymmetric MHD equilibrium neglects the inductive response of the plasma to the applied fields. Shielding of resonant perturbations can occur due to plasma rotation [17], or more generally, by the

parallel currents induced by nonideal force-balance [18]. On the other hand, if the plasma is close to a stability boundary, the applied fields can actually be amplified by the plasma response [19]. Rotation may be playing a crucial role, since these plasmas rotate quickly due to NBI heating, $\Omega_\phi \sim 5$ kHz, and actually spin up as the density drops and the ELMs disappear. This contrasts with the moderate-collisionality experiments [1,2] where rotation decreases after RMP application as expected. In principle, self-consistency can be improved by iterating E3D with a code that is capable of determining the linear plasma response to a given set of perturbations. Future development will include plasma response models.

The E3D two-fluid code has been applied to 3D simulation of low-collisionality RMP ELM suppression experiments on DIII-D. Evidence for the predicted homoclinic tangle was found in D_α-filtered images of the divertor target, but the resulting parallel electron heat transport was too large to match experimental results. In this work, we have focused solely on the geometric effect of chaotic magnetic field lines on thermal transport in the fluid regime. Thus, the disagreement may either be due to incomplete physical modeling or it may be due to incomplete assumptions about the perturbed magnetic field. The present study cannot definitively reach either conclusion, but this is clearly a subject for future research that may yield to 3D edge modeling tools. Quantitative treatment may eventually require kinetic modeling to accurately represent the nonlocal parallel heat transport in the collisionless pedestal. At the edge of the H-mode plasma, the complete response will be determined by the subtle interplay among rotation, turbulence, and ambipolar transport.

Acknowledgments

This work was supported by U.S. Department of Energy under DE-FC02-04ER54698, DE-FG02-05ER54809, DE-FG02-04ER54758 and W-7405-ENG-48. I. Joseph and R. Moyer would also like to thank the Max Planck Insitut für Plasmaphysik and EURATOM for

providing accommodations in Greifswald, Germany and for providing continued supercomputing support.

References

[1] R.A. Moyer, T.E. Evans, T.H. Osborne, et al., Phys. Plasmas **12** (2005) 056119.

[2] T.E. Evans, R.A. Moyer, J.G. Watkins, et al., Nucl. Fusion **45** (2005) 595.

[3] K.H. Burrell, T.E. Evans, E.J. Doyle, et al., Plasma Phys. Control. Fusion **47** (2005) B37.

[4] T.E. Evans, K.H. Burrell, R.A. Moyer, et al., Nature Phys. **2** (2006) 419.

[5] T.E. Evans, R.A. Moyer, and P. Monat, Phys. Plasmas **9** (2002) 4957.

[6] A.M. Runov, D. Reiter, S.V. Kasilov, et al., Phys. Plasmas **8** (2001) 916.

[7] A.M. Runov, S. Kasilov, R. Schneider, et al., Contrib. Plasma Phys. **44** (2003) 18.

[8] L.L. Lao, H.E. St. John, R.D. Stambaugh, et al., Nucl. Fusion **25** (1985) 1611.

[9] T. Rognlien, J. Milovich, M. Rensink, and G. Porter, J. Nucl. Mater. **196-198** (1992) 347.

[10] B.J. Braams, P.J. Harbour, M.F.A. Harrison, et al. J. Nucl. Mater. **121** (1984) 75.

[11] R.J. Groebner, M.A. Mahdavi, A.W. Leonard, et al., Nucl. Fusion **44** (2004) 204.

[12] R.A. Moyer, J.W. Cuthbertson, T.E. Evans, et al., J. Nucl. Mater. **241-243** (1997) 633.

[13] V.K. Melnikov, Trans. Moscow Math. Soc. **12** (1963) 1.

[14] T.E. Evans, R.K.W. Roeder, J.A. Carter, et al., J. Phys. Conf. Ser. **7** (2005), 174.

[15] T.E. Evans, I. Joseph, R.A. Moyer, M.E. Fenstermacher, C.J. Lasnier, L. Yan, "Experimental and numerical studies of separatrix splitting and magnetic footprints in DIII-D," to be presented at the 17th Plasma Surface Interactions in Controlled Fusion Devices, Hefei, China, 2006.

[16] A.B. Rechester and M.N. Rosenbluth, Phys. Rev. Lett. **40** (1978) 38.

[17] R. Fitzpatrick, Phys. Plasmas **5** (1998) 3325.

[18] A.H. Boozer, Phys. Plasmas **12** (2005) 092504.

[19] A.H. Boozer, Phys. Rev. Lett. **86** (2001) 5059.

Figure captions

Fig. 1. Poincaré plot of 10 TRIP3D magnetic field line trajectories for 1000 toroidal transits for shot #122342 at 4650 ms with I-coil and C-coil. Also shown are the EFIT flux surfaces, EFIT separatrix, DIII-D inner vacuum vessel, and I-coil positions (red circles).

Fig. 2. The electron temperature contours computed by E3D closely follow the invariant manifolds that emanate from the X-point. The stable/unstable manifold oscillates wildly as it connects to the divertor target on the right/left hand side of the figure. The oscillatory behavior in T_e is an aritifact of interpolation.

Fig. 3. D_α filtered tangential X-point TV images show multiple stripes on the inner strike point during the $n = 3$ I-coil current pulse in shot #123301 at 2171 ms. Only a single stripe is observed both before and after the I-coil pulse.

Fig. 4. 2D electron temperature distribution predicted by E3D on the $\phi = 0$ plane for varying levels of even-parity I-coil current: 0, 1, 2, 3 kA. The separatrix tangle structure grows while the pedestal cools with increasing RMP strength.

Fig. 5. The electron temperature pedestal sampled at the experimental Thomson scattering measurement location is predicted to cool as the I-coil current is scanned from 0 to 3 kA. The purple curve corresponds to the experimental settings: I-coil = 3 kA and C-coil = 12 kAt shown in Fig. 1.

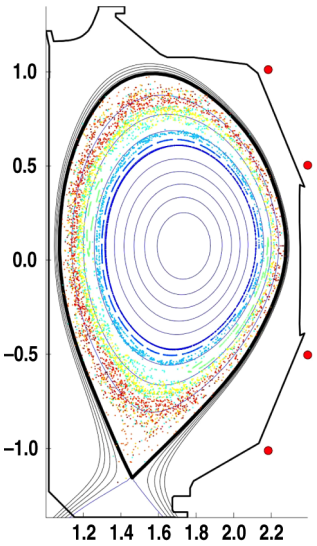

Fig. 1, I. Joseph et al., P3-11

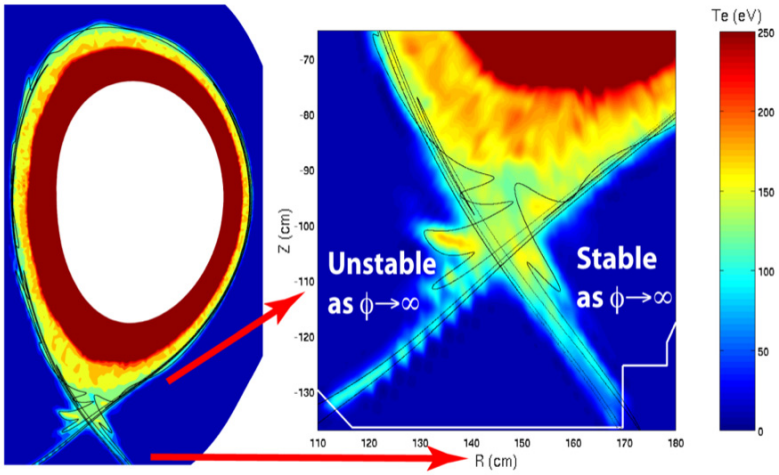

Fig. 2, I. Joseph et al., P3-11

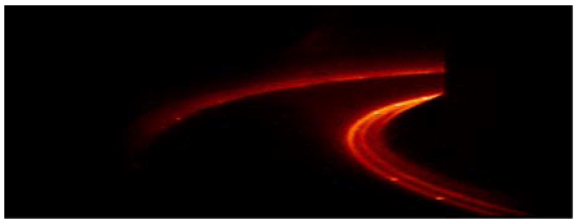

Fig. 3, I. Joseph et al., P3-11

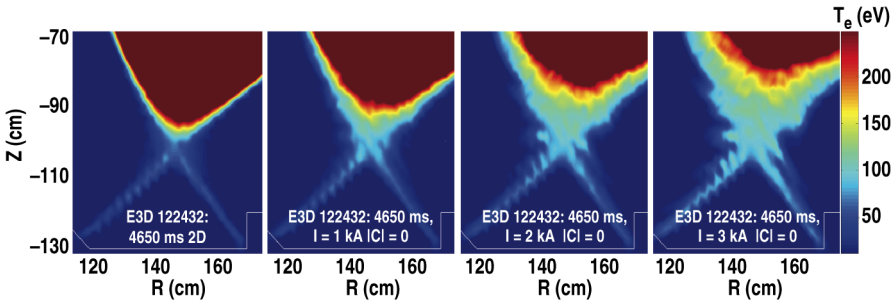

Fig. 4, I. Joseph et al., P3-11

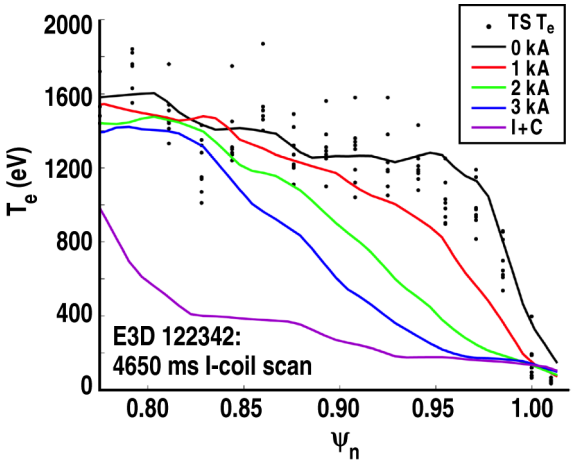

Fig. 5, I. Joseph et al., P3-11